

Multispectral imaging system with interchangeable filter design

Michio Kise^{a,*}, Bosoon Park^b, Gerald W. Heitschmidt^b, Kurt C. Lawrence^b, William R. Windham^b

^a John Deere Technology Innovation Center, 2021 S. First St., Suite 101, Champaign, IL 61820, United States

^b USDA-ARS, 950 College Station Road, Athens, GA 30605, United States

ARTICLE INFO

Article history:

Received 15 April 2009

Received in revised form 25 January 2010

Accepted 22 February 2010

Keywords:

Multispectral imaging system

Optical system design

Interchangeable filter

Image calibration

ABSTRACT

The design and calibration of a three-band image acquisition system was reported in this paper. The prototype system developed in this research was a three-band spectral imaging system that acquired two visible-band images and one NIR image simultaneously. This was accomplished by using a three-port imaging system that consisted of three identical monochrome cameras, an optical system, and three interchangeable optical filters. Spectral reflectance from an object was collimated by a front lens, and split in three ways by a cold mirror and beamsplitter: a cold mirror reflects 90% visible light and transmits 80% NIR light. The visible light was again split identically into two directions by an additional beam-splitter. Focusing lenses then projected each image onto its corresponding sensor. By incorporating an interchangeable filter design, the imaging system can measure any two visible spectral bands that range between 400 nm and 700 nm, and one NIR band that ranges between 700 nm and 1000 nm without any complicated manufacturing process. In order to co-register the three images, a system-specific calibration algorithm was developed that compensates for lens–sensor geometric misalignments.

The prototype imaging system and the system calibration algorithm were tested and evaluated for image alignment accuracy. The imaging system acquired three-band images of 3D objects with 0.39 pixel misalignment error on average.

© 2010 Elsevier B.V. All rights reserved.

1. Introduction

Spectral imaging is designed to acquire images at specific spectral bands with the purpose of measuring the spectral characteristics of objects in a non-destructive manner. This is based on the concept that different materials absorb and reflect light energy in different proportions at different wavelengths, thus producing characteristic spectral patterns. This has permitted researchers to investigate a variety of agricultural phenomena. For example, typical remote sensing applications using the visible to near-infrared (Vis/NIR) region include plant growth monitoring and crop yield prediction from airborne platforms (Yang et al., 2004), food safety and quality inspection (Heitschmidt et al., 2007; Kawamura et al., 2007), and fruit maturity detection (Noh et al., 2007) using bench-top systems.

If a spectral imaging system collects about 2–10 different spectral bands, it is often called multispectral imaging. Multispectral imaging may not measure as many spectral bands as hyperspectral imaging that can acquire several hundred spectrally contiguous

bands (Lawrence et al., 2003). However, most multispectral imaging systems acquire spatially-coherent band images simultaneously, which makes these systems more applicable to real-time applications versus hyperspectral imaging systems. Some multispectral imaging systems use a combination of dichroic mirrors to separate the incoming light into a desired number of broad spectral bands (Duncan and Kantor, 1997; Tanikawa et al., 2000). These broad bands of light are then passed through narrow bandpass filters and the intensity of this narrow range of light is then measured by individual detectors. This method is spectrally more efficient than typical beamsplitter-based systems (Hopkins, 1999), but the choice of narrow spectral bands is limited by the combination of dichroic mirrors incorporated by the system. Therefore, it is difficult to change narrow spectral bands once the dichroic coatings are determined and installed. Furthermore, multispectral imaging systems need very precise optical alignment for band-to-band image registration.

Therefore, the objective of this study was to develop a compact, cost-effective, and spectrally flexible multispectral camera system that could measure two visible bands and one NIR band simultaneously. The system design incorporated interchangeable filters, beamsplitters, and three digital monochrome cameras. Such a design has a great advantage over multispectral imaging systems that integrate filters and sensors as a complete module because it offers greater flexibility with respect to spectral band selection. With this improved flexibility, our system can be retrofitted

* Corresponding author. Tel.: +1 217 819 5218; fax: +1 217 819 5226.

E-mail addresses: KiseMichio@JohnDeere.com (M. Kise),

bosoon.park@ars.usda.gov (B. Park), jerry.heitschmidt@ars.usda.gov (G.W. Heitschmidt), kurt.lawrence@ars.usda.gov (K.C. Lawrence), bob.windham@ars.usda.gov (W.R. Windham).

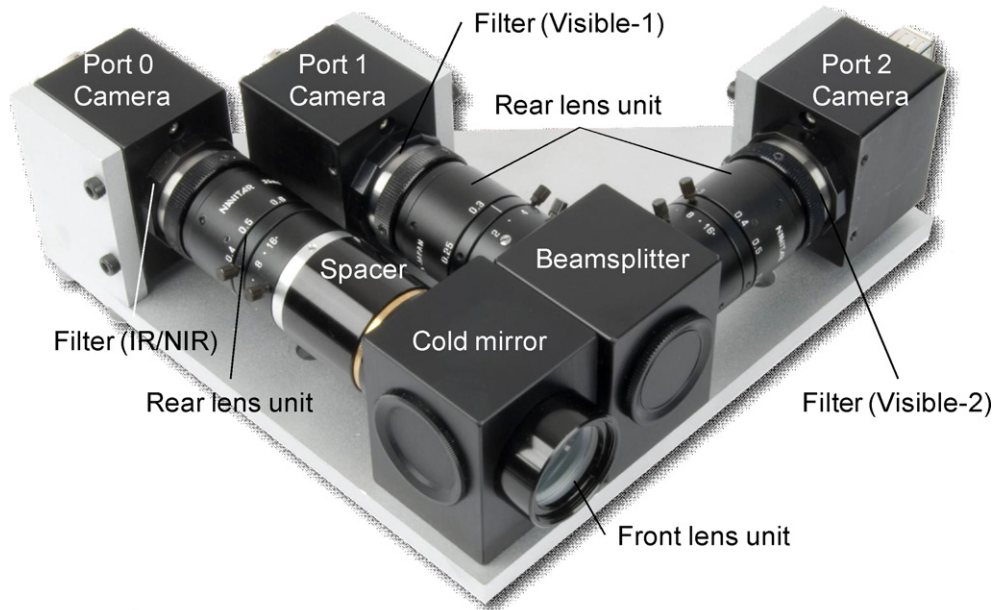


Fig. 1. Three-band spectral imaging system.

for a variety of applications, such as handheld devices for food safety and quality inspection (Kise et al., 2008), airborne remote sensing – especially for a small unmanned aerial vehicle with limited payload capacity (Sugiura et al., 2005). This paper reports the optical design of the multispectral camera system, the calibration algorithm that compensates for optical misalignment, and a case study of the imaging system applied to food contaminant detection.

2. Design of three-band imaging system

Fig. 1 shows that the three-band spectral imaging system in this research consisted of three identical monochrome cameras, a cold mirror, a beamsplitter, lenses, and three optical filters. To develop the system in a cost-effective manner, the entire system was designed and assembled with off-the-shelf products. The monochrome cameras (EC1380, Prosilica, British

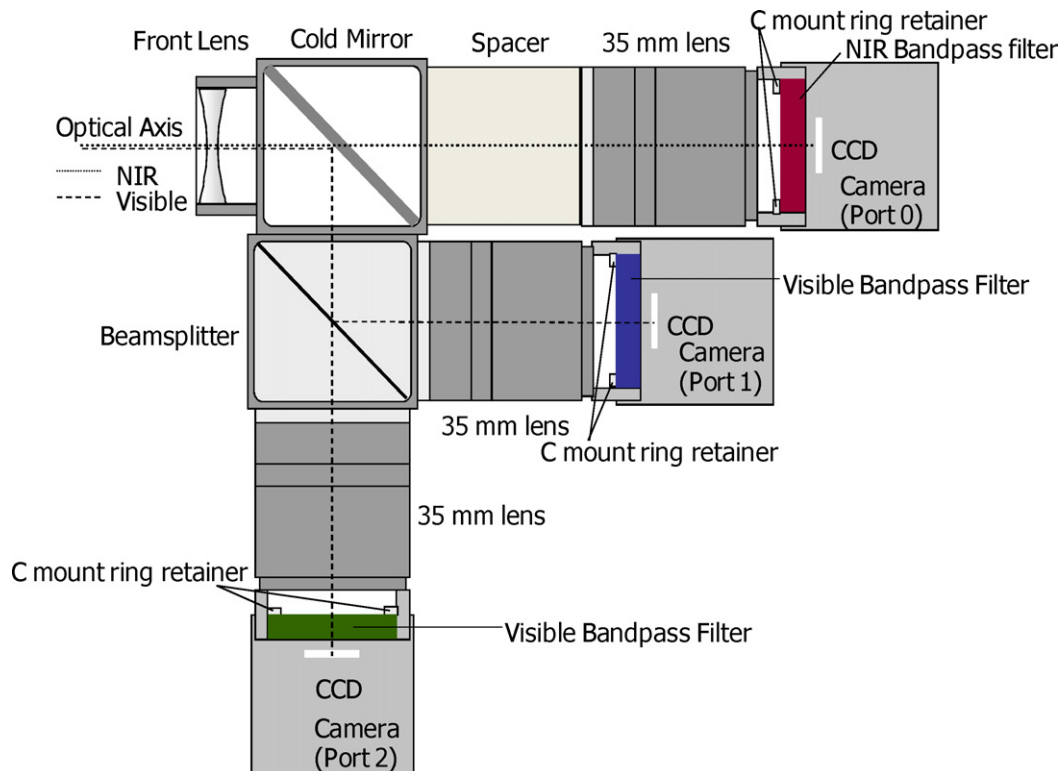


Fig. 2. Optical diagram of the three-band spectral imaging system.

Columbia, Canada) were equipped with 2/3 in. CCD's that acquired 1360 pixel \times 1024 pixel, 12-bit monochrome images at up to 10 frames per second. Spatial binning was set at 2×2 for all imagery acquired in this study. These settings resulted in 680 pixel \times 512 pixel images. The camera accepted C-mount components and had an IEEE1394A (FireWire, 393.216 Mbit/s) port for data communication. All three cameras were connected to the same FireWire bus.

Image capturing from the three cameras was synchronized by an external trigger. An external trigger generator was developed based on a micro-controller (PIC16F877, Microchip, Chandler, AZ) which generated three identical TTL signals. The system calibration algorithm was programmed in a C++ environment (Microsoft Visual Studio 2005, Microsoft, Redmond, WA) and loaded on a notebook computer (Dell Latitude D420, Pentium 4, 3.2 GHz, 1 GB RAM, Windows XP Professional). The three cameras were connected to the PC's onboard FireWire port via a 4-port FireWire hub (HFW410, Koutech Systems, Inc., Industry, CA).

Fig. 2 shows the optical diagram of the three-band spectral imaging system. The optical components of the imaging system consisted of a front lens unit, a cold mirror, a beamsplitter, three bandpass filters and three rear lens units. The front lens unit was a negative achromatic lens (25 mm diameter \times –30 mm focal length) (NT48–351, Edmund Optics, Barrington, NJ). The lens was enclosed in a C-mount lens holder that had a C-mount male thread at the base end (NT56–354, Edmund Optics, Barrington, NJ). Incident light was collimated by the front lens, and then split into two paths by a cold mirror (NT62–642, Edmund Optics, Barrington, NJ), which reflects 90% of visible light and transmits 80% of infrared/near-infrared (IR/NIR) straight through. The visible component was further split in half by a cube-beamsplitter (NT49–682, Edmund Optics, Barrington, NJ) which reflected 50% of the light at right angle and transmitted the other 50% straight through. To compensate for optical path differences between visible and IR/NIR components, a spacer that had a same optical length as that of the beamsplitter was attached behind the cold mirror of IR/NIR port.

Identical rear lens configurations focused the images onto the CCD sensor of each camera. A C-mount lens (35HB, Tamron, Saitama, Japan) was used for each of the rear lens units and was attached backward on each camera's mount. Each lens had a fixed focal length of 35 mm. Both the focus and iris could be adjusted manually. Since each port image was the product of a unique narrow bandpass filter, the ability to focus independently was critical to optimizing the image quality.

A narrow bandpass optical filter was mounted within each camera by a C-mount ring retainer. This design granted easy access to the filters, thus allowing the system to be retrofitted for a variety of applications. Three narrow bandpass interference filters with a 24.1 mm diameter were implemented for poultry contaminant detection (Park et al., 2005): two visible filters had central wavelengths (CWL) at 510 nm, and 568 nm with 10 nm full-width at half-maximum (FWHM), respectively. The NIR filter had 800 nm CWL and 40 nm FWHM. The paraxial specifications of the imaging system are summarized in Table 1. With current front–rear lens configuration, the system yielded 13.7 mm of system focal length. However the system focal length was configurable by choosing appropriate front lens with different focal lengths (Kise et al., 2007).

2.1. Image misalignment error

One of the technical challenges in developing this type of multi-camera system was obtaining precise optical alignment. Because the pixel size of the image sensors was about 5 μ m, it required optical alignment precision that was in the millimeter to micro-millimeter range in order to gain acceptable sub-pixel image alignment accuracy.

Table 1

Optical system paraxial specifications.

Front lens	–30 mm negative achromatic doublet, 25 mm diameter
Back lens	35 mm fixed focal lens, manual focus, manual iris, F-stop: 2.1–22
Cold mirror	Substrate: BOROFLOAT™, thickness: 3.3 mm, reflectance: 90% visible light, transmission: 80% IR waves
Beamsplitter	Material: BK7, transmit and reflect: 50% \pm 5% at 550 nm, cube size: 35 mm
System focal length	13.7 mm
Working F#	7.7
Stop radius	2.0 mm
Physical distance from front lens to CCD	106 mm

Fig. 3 shows that the raw images taken by the three-band spectral imaging system suffered from significant image misalignment. The images in Fig. 3 show a fixed frequency grid distortion target that consisted of an array of dots with 1 mm diameter and 5 mm spacing. These images were taken by the imaging system at a 50 cm working distance. Fig. 3(a)–(c) shows the original images acquired by port-0 (NIR), port-1 (visible-1) and port-2 (visible-2) of the imaging system, respectively. Fig. 3(d) is a composition of the port-0 and port-1 images where all dots in the image of port-0 were superimposed onto the image from port-1. The composite image demonstrated significant image-to-image misalignment; the large offset was easily recognized by comparing the location of the large dot near the center of the image. The offset of the large (center) dots was 122.8 pixels between port-0 and port-1, and 24.6 pixels between port-1 and port-2, respectively.

Misalignment of the resulting imagery was largely due to imprecision encountered during the hardware assembly process. The optical components, including lenses and mirrors, could not be perfectly aligned without special fabrication. In particular, the significant offset of image-0 was caused by misalignment of the cold mirror mounting.

In addition, inconsistencies in the camera's sensor position contributed to image misalignment. As determined by the manufacturer, each camera's CCD sensor had a positional tolerance of about $\pm 250 \mu$ m. Considering the size of a pixel on the sensor (12.9 μ m for 2×2 binning), the sensor positioning tolerance alone could result in approximately a ± 19 -pixel offset between the two images.

Finally, the quality of the lenses also contributed to image misalignment. A severe negative (barrel) distortion was apparent in the images. Even though the three rear lens units had an identical design, the images formed by each rear lens unit were slightly different because of lens manufacturing tolerances. Such manufacturing tolerances also had to be taken into account (Fischer and Tadic-Galeb, 2000).

The images in Fig. 3 also reveal that the optical system suffered from severe vignetting that caused dark or even entirely black areas around the perimeter of the image. Such vignetting was the result of the ray bundles from certain points in the field-of-view of the sensor being partially or entirely truncated by the iris of the optical system. Clearly, the maximum field-of-view of the optical system was smaller than the 2/3 in. CCD sensors (8.78 mm \times 6.60 mm) of the imaging system.

The rectangles in each image of Fig. 3 represent the field-of-view of a 1/2 in. image sensor (6.58 mm \times 4.95 mm). The figure suggests that the field-of-view of the optical system was large enough for a 1/2 in. sensor or smaller. It should be noted that a 2/3 in. sensor would still be required to yield a 1/2 in. field-of-view in order to provide sufficient image overlap among the three sensors.

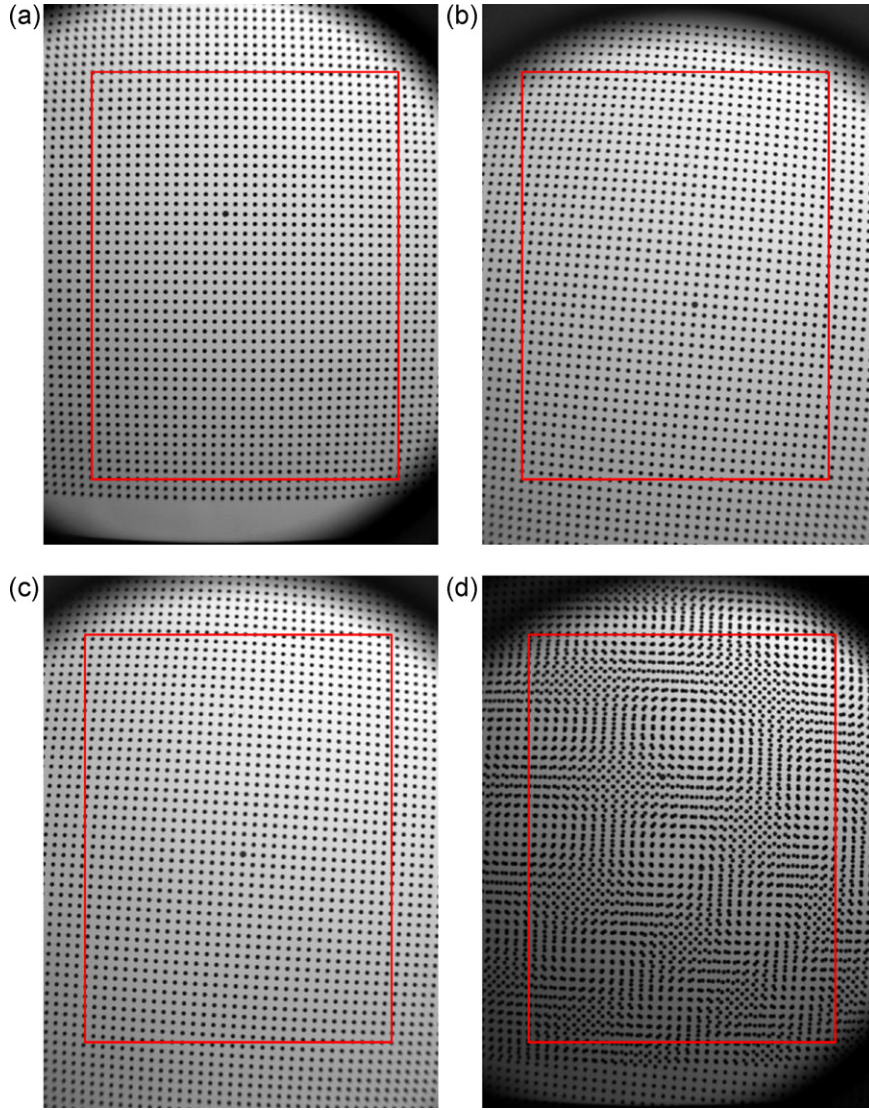


Fig. 3. Images of grid distortion target taken by the three-band spectral imaging system. (a) Image of port-0 (NIR). (b) Image of port-1 (visible-1). (c) Image of port-2 (visible-2). (d) Overlay image of port-0 with the image of port-1. Rectangles in each image indicated the size of 1/2 in. sensor.

2.2. Image calibration algorithm

We have proposed a camera calibration algorithm for image-to-image misalignment correction in a previous report (Kise et al., 2007). The proposed algorithm was a two-step process in which two types of error, a lens distortion error and a sensor positioning error, were corrected consecutively. Lens distortion was corrected by applying a mathematical lens distortion model to the original image. Sensor positioning error was then corrected by projecting one image onto another image using a linear projection. The performance evaluation revealed that even though the calibration could remove the majority of misalignment, in the case of severe lens distortion some image misalignment was still evident.

In this paper, a new calibration method is proposed. Instead of relying on the mathematical models, the new method incorporates a measurement-based, non-linear image transformation method. Each pixel's offset error between two images is determined based on direct measurements. By comparing a known patterned image, such as the distortion grid target shown in Fig. 3, the misalignment error at several locations in the image can be directly measured. It is assumed that the misalignment error is continuous across the image such that the error at any given point can be interpolated from the neighboring points.

Let us consider the case where an image from port-2 is transformed onto the image coordinates from port-1. If a given point in the port-1 image, $m_1 = (i_1, j_1)$ and another given point $m_2 = (i_2, j_2)$ in port-2 image, represent the same point on the target, the misalignment error at point m_2 is expressed by:

$$d(m_2) = m_1 - m_2 = \begin{pmatrix} i_1 - i_2 \\ j_1 - j_2 \end{pmatrix} \quad (1)$$

It is virtually impossible to measure error d at all pixels directly. However, it is reasonable to assume that such an error is spatially continuous, thus permitting interpolation based on neighboring pixels.

$$\hat{d}(m_2) = \sum_{x \in S} w(x) \bar{d}(x) \quad (2)$$

where $\hat{d}(m_2)$ is the estimation of the misalignment error at m_2 , $\bar{d}(x)$ is an observation of the misalignment error at neighboring pixel x , and $w(x)$ is the weight. The set S represents the neighborhood whose size is defined by its radius r . Observed points that are located close to the point to be interpolated are weighed heavily, while those further away are weighed lighter. A Gaussian-based parameter, which drops off as a Gaussian distribution with distance

from the missing data value, is used as the weight.

$$w(x) = \frac{\omega(x)}{\sum_{i \in S} \omega(i)} \quad (3)$$

$$\omega(x) = \frac{1}{\sqrt{2\pi}\sigma} \exp\left(-\frac{D(x)^2}{2\sigma^2}\right)$$

$$D(x)^2 = |m_2 - x|^2$$

where σ is the standard deviation of the Gaussian function. In our algorithm, the value σ was designated as 10 (pixels). This value was based on the approximate grid size in the distortion target images. This ensured that at least four observed points would be found within σ (pixels) from any given pixel in the image. It also should be noted that the effectiveness of the radius r was dictated by the weight $w(x)$ because the weight became almost zero after the $D(x)$ increased over a certain distance. In our research, the radius of the neighborhood S was set at 3σ ($r=3\sigma$).

The images of the grid distortion target shown in Fig. 3 were used for the calibration. Fig. 4 shows a flowchart for the creation of a projection map. A GUI-based projection map creation programme was developed using Microsoft Visual C++ 2005. In this example, a port-1 image was used as the base image onto which port-0 and port-2 images were projected. After the three-band image was taken, the image from port-1 was converted into a binary image by applying an appropriate threshold. A spatially dynamic threshold value was used to compensate for the spatial variability of the illumination.

$$T(x, y) = \sum_{i=x-l}^{x+l} \sum_{j=y-l}^{y+l} \frac{g(i, j)}{(2l+1)^2} \quad (4)$$

where $T(x, y)$ is the threshold value at pixel (x, y) , $g(i, j)$ is the gray level of the image at pixel (i, j) , l is the size of the square window, and p is a constant parameter that can be adjusted manually. The basic idea of Eq. (4) was that the threshold value could be determined based on the average of the gray levels of neighboring pixels and could be adjusted manually with parameter p if the resulting binary image did not effectively distinguish the dots from the background. Initial value of p was set at 0.6.

If necessary, spatial filters were applied to the resulting binary images to ensure the fidelity of the dots. These included both open-

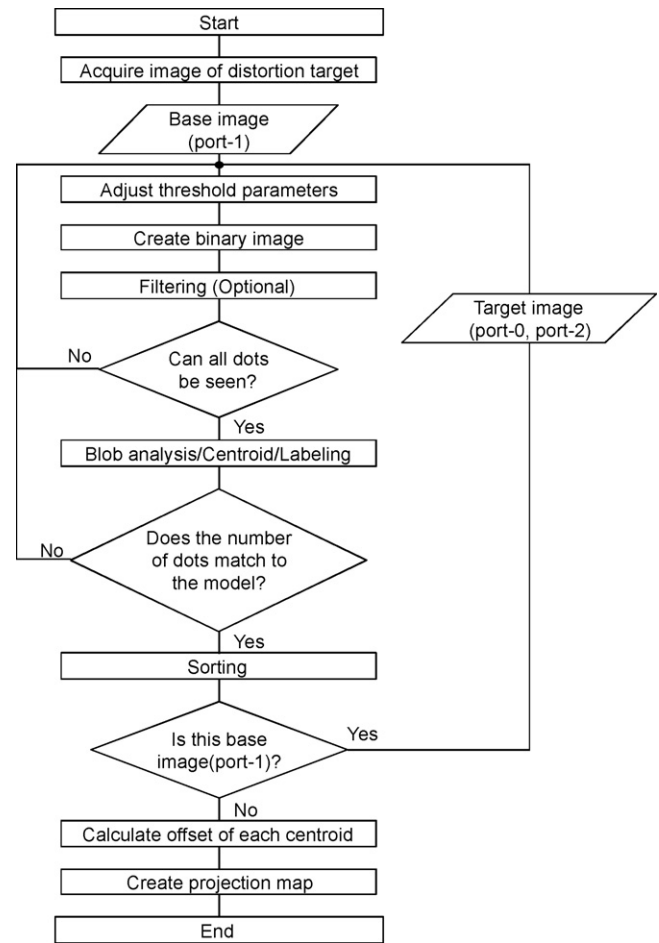


Fig. 4. Flowchart of projection map creation.

ing and closing filters. In a few extreme cases, manual editing was required to produce optimal results.

The centroids of all of the dots in the binary images were determined by performing a blob analysis that included both centroid determination and labeling. If the number of centroids did not match the number of the dots in the distortion target,

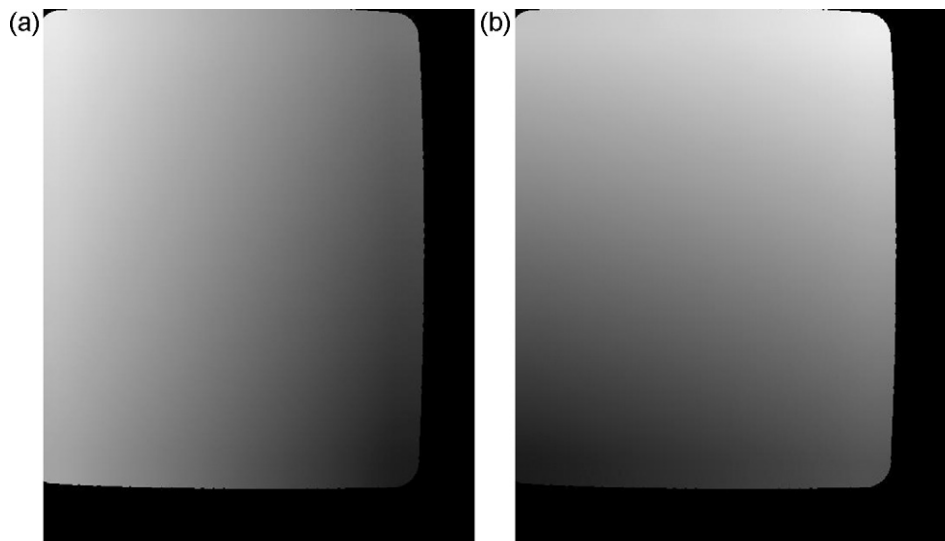


Fig. 5. Image projection maps used to transform the port-0 image to the port-1 image coordinates. Gray level at each pixel represents misalignment error in pixel. (a) Projection map in x direction. (b) Projection map in y direction.

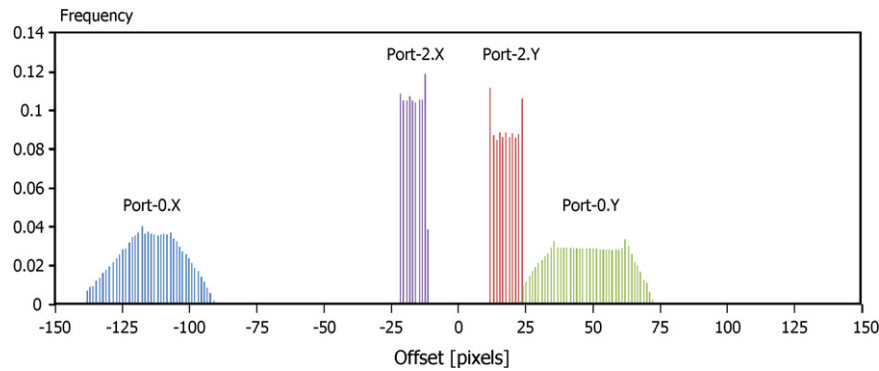


Fig. 6. Histogram of projection maps (offset of each image).

it went back to the image-binarize-process with new threshold value. If it matched, a sorting algorithm was applied to the list of centroids. The sorting algorithm scanned the image from the left-bottom corner in a horizontal direction until the right-top dot was found. Because of this scanning algorithm, it was important for the distortion target image to be captured with minimal rotation.

After the centroids in the base image (port-1) were detected and sorted successfully, the target images (port-0 and port-2) were processed in the same fashion. Then corresponding centroids were determined automatically, given that the centroids in the three images were sorted correctly. Next, the misalignment error at each centroid was calculated and four projection maps (two projection maps for each port image pair, port-0-to-port-1 and port-2-to-port-1) were created using Eq. (2). These maps contain estimates of the misalignment errors at all pixels.

Fig. 5 shows the resulting image projection maps used to transform the port-0 image to the port-1 image coordinates. Each port image required two projection maps, one for both the x and y directions. The image projection maps were stored in the form of 16-bit monochrome image. The range of the offset value projection maps represented was set at ± 150 pixels. Based on the fact that the offset of the large dots between port-0 image and port-1 image was about 120 pixels, ± 150 pixels was considered to be large enough to represent the maximum offset. Black pixels in the maps indicate that no corresponding points were found in that area due to the limited overlap between the images. The projection map shows a smooth, gradient-like texture which reveals its spatial continuity.

Fig. 6 shows the histograms of port-0 and port-2 projection maps. This plot reveals that the offsets of the port-0 image had not only larger offsets than the port-2 image, but also a larger error distribution. The difference was due to their different optical paths, where the path of port-0 was split first from the path of port-1 and port-2 by the cold mirror. In other words, the image misalignment error caused by the cold mirror mounting only affected port-0 – not port-2. Table 2 summarizes the error of each projection map. Table 2 confirms that the offset error of port-0 was significantly larger than that of port-2.

Table 2
Projection map error.

	Min [pixels]	Max [pixels]	Range [pixels]	Average [pixels]
Port-0.X	-137	-90	47	-114
Port-0.Y	23	72	49	48
Port-2.X	-22	-11	11	-17
Port-2.Y	11	25	14	-12

Table 3
Misalignment after the calibration.

Distance [cm]	Average [pixel]	Max [pixel]
40	0.48	0.98
50	0.40	1.00
60	0.35	0.94
70	0.32	1.05
Total	0.39	1.05

3. Results and discussions

A series of three-band images were collected to evaluate the system's calibration accuracy. With the imaging system fixed on an optical table, a distortion target was placed perpendicular to the optical axis of the imaging system at four different object distances using 10 cm intervals. Images were taken at each distance and subsequently calibrated by the previously described method. The



Fig. 7. Example of the calibration result. Composite image of grid distortion target and 3D object.

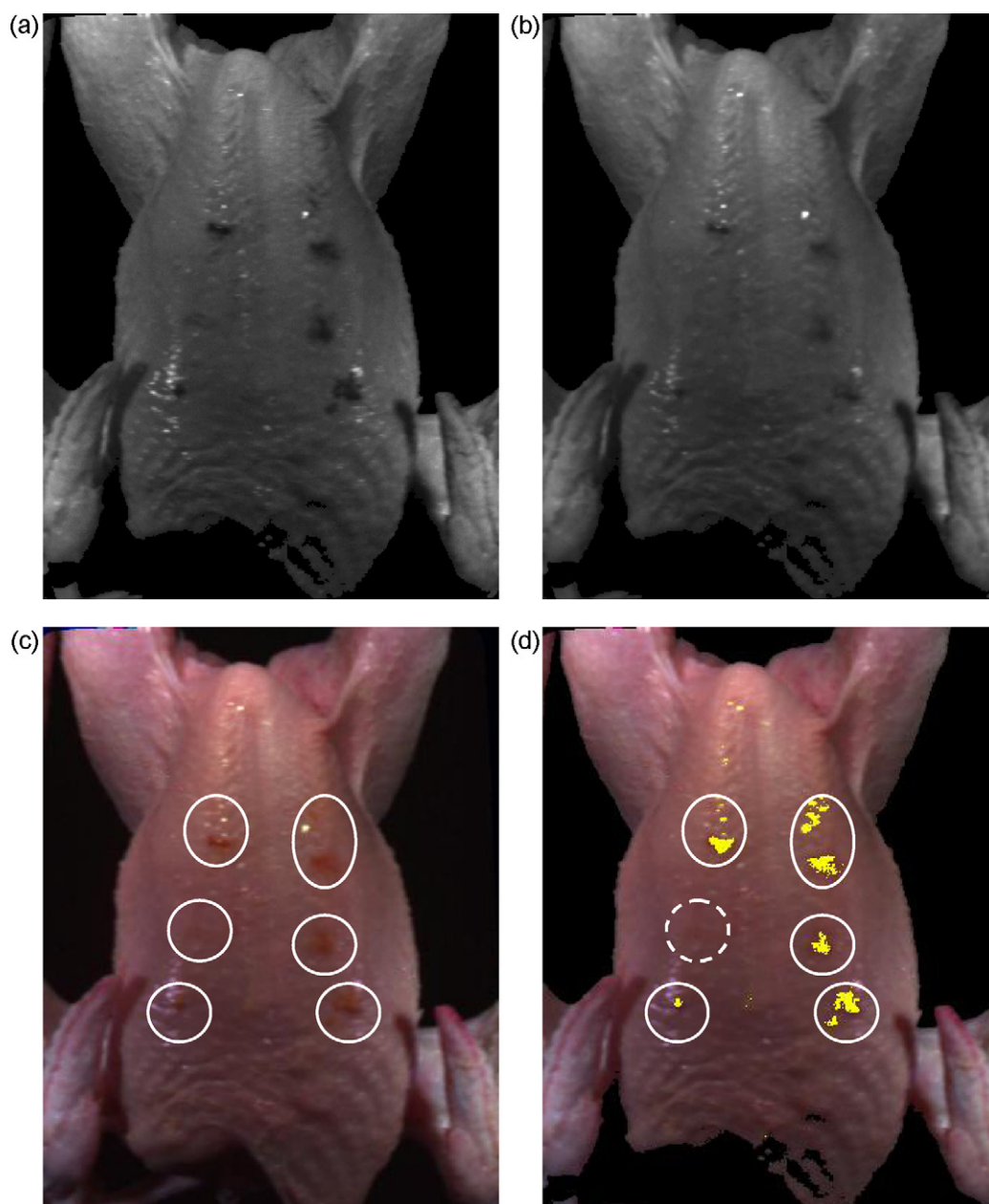


Fig. 8. Result of poultry contaminant detection; (a) Image of port-1 (510 nm). (b) Image of port-2 (568 nm). (c) Fecal contaminants were manually deposited at six spots on the carcass surface (circles indicated contaminated spots). (d) Result of the contaminant detection with threshold $T = 1.2$. One spot (shown in broken circle) was undetected.

distance between corresponding centroids of each dot in the calibrated images was calculated as the image misalignment error. The test results are summarized in Table 3. Overall, very similar results were found at all object distances tested (40 cm, 50 cm, 60 cm and 70 cm). The average error across the image was 0.32 pixels ($5.03 \mu\text{m}$).

The results shown in Table 3 indicate that the calibration algorithm worked consistently regardless of the scene depth or angle. This was possible because our calibration algorithm used pre-determined offset values for individual pixels. In other words, the offsets were already determined before the images were captured. This represented a significant advantage compared to dynamic pixel matching algorithms, such as stereovision, where accuracies are subject to the scenes.

Fig. 7 shows an example of the calibration result. It demonstrates that the misalignment of the distortion target images, which was apparent in Fig. 3, has been corrected; all dots were accurately

aligned over three images. The composite image shows that all three images were precisely aligned over the entire region of interest (ROI), in which the calibration target and a 3D object (a stuffed bear) were placed at a short distance.

One of the possible applications for our multispectral imaging system is as a compact inspection tool for food contaminant detection. Fig. 8 shows an image of a chicken carcass taken by the imaging system along with the detection results based on a band-ratio algorithm. Four types of contaminant materials (duodenum, cecum, colon, and ingesta) were manually deposited at the six spots on the chicken carcass indicated by circles (Fig. 8(c)). Background pixels with a reflectance of less than 2.5% were masked out, and a ratio of the two images (568 nm/510 nm) was calculated. A threshold ($T = 1.2$) was then applied to the ratio of the two images to identify fecal and ingesta contaminants. Yellow pixels in the image (Fig. 8(d)) indicate where the ratio results surpassed the threshold, thus revealing presumed fecal contamination. Overall, the result

demonstrated that the five of six contaminated spots were successfully discriminated from the skin. Additional fecal detection testing showed that the prototype system could determine the presence or absence of fecal contaminants on chicken carcass. However, further investigation and testing should be conducted to assess the accuracy and feasibility of the application.

4. Conclusion

A prototype three-band spectral imaging system was developed and evaluated. The imaging system could acquire three-band images in user-selected spectral bands (two visible and one NIR) simultaneously by utilizing three interchangeable optical filters, three monochrome cameras, and various optical components. Raw band-images captured by the three-band spectral imaging system suffered from image-to-image misalignment, as was expected. To compensate for sensor-lens positioning misalignment, a calibration algorithm was developed. The calibration algorithm could correct the alignment of three-band images with only a 0.39-pixel (5.03 μm) error. Our prototype three-band spectral imaging system is low-cost, compact, and spectrally flexible. Preliminary tests showed that it could produce a quality three-band spectral imagery. Accordingly, our system can be retrofitted for a variety of imaging applications, ranging from handheld applications to use as an onboard sensor for small unmanned aerial vehicles.

Acknowledgements

The authors would like to thank Alan Savage, Engineering Technician and Peggy Feldner, Food Technologist, for their assistance in developing the system and conducting the tests.

References

- Duncan, D.B., Kantor, S., 1997. Spectral imaging method and apparatus. US Patent No. 5 677 532.
- Fischer, R.E., Tadic-Galeb, B., 2000. Optic System Design. McGraw-Hill, New York, NY.
- Heitschmidt, G.W., Park, B., Lawrence, K.C., Windham, W.R., Smith, D.P., 2007. Improved hyperspectral imaging system for fecal detection on poultry carcasses. Transactions of the American Society of Agricultural and Biological Engineers 50 (4), 1427–1432.
- Hopkins, M.F., 1999. Multi-spectral two dimensional imaging spectrometer. US Patent No. 5 926 283.
- Kawamura, S., Kawasaki, M., Nakatsuji, H., Natsuga, M., 2007. Near-infrared spectroscopic sensing system for online monitoring of milk quality during milking. Sensing and Instrumentation for Food Quality and Safety 1 (1), 37–43.
- Kise, M., Park, B., Lawrence, K.C., Windham, W.R., 2007. Design and calibration of a dual-band imaging system. Sensing and Instrumentation for Food Quality and Safety 1 (3), 113–121.
- Kise, M., Park, B., Lawrence, K.C., Windham, W.R., 2008. Development of handheld two-band spectral imaging system for food safety inspection. Biological Engineering 1 (2), 145–157.
- Lawrence, K.C., Park, B., Windham, W.R., Mao, C., 2003. Calibration of a pushbroom hyperspectral imaging system for agricultural inspection. Transactions of the American Society of Agricultural and Biological Engineers 46 (2), 513–521.
- Noh, H.K., Peng, Y., Lu, R., 2007. Integration of hyperspectral reflectance and fluorescence imaging for assessing apple maturity. Transactions of the American Society of Agricultural and Biological Engineers 50 (3), 963–971.
- Park, B., Lawrence, K.C., Windham, W.R., Smith, D.P., 2005. Multispectral imaging system for fecal and ingesta detection on poultry carcasses. Journal of Food Process Engineering 27 (5), 311–327.
- Sugiura, R., Noguchi, N., Ishii, K., 2005. Remote-sensing technology for vegetation monitoring using an unmanned helicopter. Biosystems Engineering 90 (4), 369–379.
- Tanikawa, K., Okamura, T., Kudo, J., Wada, H., Shirahata, H., 2000. Six band multi-spectral sensor using off-axis three mirror reflective optics. Optical Engineering 39 (10), 2781–2788.
- Yang, C., Everitt, J.H., Bradford, J.M., 2004. Airborne hyperspectral imagery and yield monitor data for estimating grain sorghum yield variability. Transactions of the American Society of Agricultural and Biological Engineers 47 (3), 915–924.